Chemical Engineering Journal 102 (2004) 151–160

Chemical Engineering Journal

www.elsevier.com/locate/cej

Numerical study of gas–solid flow in a precalciner using kinetic theory of granular flow

Liu Huanpeng [a], Liu Wentie [a], Zheng Jianxiang [a], Jianmin Ding [b], Zhao Xiujian [c], Lu Huilin [a,*]

[a] *School of Energy Science and Engineering, Harbin Institute of Technology, Harbin 150001, China*
[b] *Agere Systems Inc., 555 Union Boulevard, Allentown, PA 18109-3286, USA*
[c] *Key Laboratory for Silicate Materials Science and Engineering of Ministry of Education, Wuhan University of Technology, Wuhan 430070, China*

Received 25 August 2003; accepted 12 March 2004

Abstract

A numerical study was performed for the influence of various physical parameters on the hydrodynamics of gas–solid two-phase flow in a precalciner. An Eulerian continuum two-fluid model is applied for both the gas phase and the solid phase. The transport properties of the solid phase are represented using kinetic theory of granular flow. The unsteady gas and solid flow behavior, affected by the major concerned physical parameters in the precalciner, were presented from the computer simulations. The dilute annulus-dense core flow structure of particles was predicted. The influences of the velocities of the primary and secondary jets, secondary jet arrangement, and particle–particle coefficient of restitution on the hydrodynamics of solid flow are discussed.

Keywords: Gas–solid flow; Precalciner; Kinetic theory of granular flow; Numerical simulation

1. Introduction

Thousands of small vertical precalciners dominate the Chinese cement industry. The capacity of these precalciners is very small. This hinds the increase of production of cement and causes more concerns about energy consumption and environmental pollution. Hence, optimizing and retrofitting the precalciners are required to meet the regional demands for higher-quality cement. In a general operation of precalciner, the calcined raw materials mixed with air are introduced into the precalciner column from a primary jet located at the bottom of the precalciner. The secondary air injected into the precalciners is located next to the primary jet. Coal in pulverized form is used for combustion inside the precalciner. The basic adjustable input parameters in the precalciner are the flow rates of air from the primary and secondary jets, and the mass fluxes of preheated raw materials and pulverized coal. The performance of a precalciner is evaluated by the degree of the precalcination of the raw mixture. The adjusted parameters of the mass fluxes of air and particles influence the gas–solid flow behavior and chemical reaction in the precalciner. Therefore, hydrodynamics of gas–solid flow in the precalciner is of great importance. In other words, the design and operating parameters of the precalciner affects the production of cement, energy consumption, and emission control [1,2].

Computational fluid dynamics (CFD) has become an indispensable tool for design and optimization of industrial equipments. Computational two-phase flow has been emerged as an important research area with unique characteristics and issues. Studies that examined some of the mathematical models for multiphase flow include Soo [3], Gidaspow [4], Crowe et al. [5] and Jackson [6]. With an appropriate constant solid phase viscosity, which may be empirically determined, the large-scale gas and solids flow patterns and mixing in circulating fluidized bed (CFB) risers were obtained from two-fluid model [7–9]. The kinetic theory of granular flow, based on kinetic theory of dense gases [10], yield a theoretical and solid basis for solid phase stress or viscosity. In this theory, slightly inelastic particle–particle collisions with coefficient of restitution are taken into account. The kinetic theory of granular flow has been widely used to model gas–solid flows in fluidized beds and risers, e.g. [11–17]. In present work, numerical simulations were performed to study the influence of various physical parameters on the hydrodynamics of gas–solid

* Corresponding author. Tel.: +86-10-459-6412258; fax: +86-10-459-6221048.
E-mail address: huilin@hit.edu.cn (L. Huilin).

1385-8947/$ – see front matter © 2004 Elsevier B.V. All rights reserved.
doi:10.1016/j.cej.2004.03.004

Nomenclature

C_d	drag coefficient
d	particle diameter
D	diameter of precalciner
e	restitution coefficient between particle–particle collision
e_w	restitution coefficient between particle and wall collision
g	gravity
g_0	radial distribution function
I	unit tensor
k_s	conductivity of fluctuating energy
n	normal direction
P	fluid pressure
$\mathbf{P}_s$	particle pressure
q	fluctuating energy flux
Re	Reynolds number
t	time
u_c	gas velocity of primary jet
u_{jet}	gas velocity of secondary jet
$\mathbf{v}_g$	gas velocity
$\mathbf{v}_s$	particle velocity
x	transverse distance from axis
y	vertical distance

Greek letters

β	drag coefficient
γ	collisional energy dissipation
ε_g	porosity
ε_s	particle concentration
$\varepsilon_{s,max}$	maximum concentration of solids
θ	granular temperature
μ_g	gas viscosity
μ_s	shear viscosity
ρ_s	particle density
ρ_g	gas density
τ_g	gas stress tensor
τ_s	particle stress tensor

Subscripts

c	primary jet
dil	dilute
jet	secondary jet
g	gas phase
s	solid phase

two-phase flow in the precalciner using a two-fluid model incorporated with the kinetic theory approach. Various cases of the transient gas–solid flows in the precalciner were predicted. Particle oscillations were analyzed using the power spectrum method. The effects of the primary and secondary jet velocities, secondary jet arrangement, solid flux from primary jet, and coefficient of restitution on the two-phase hydrodynamics were discussed.

2. Mathematical model and numerical solution method

2.1. Two-fluid model of gas–solid flow

The governing equations for the conservation of mass, and momentum for each phase and the constitutive relations are given in Table 1 [18]. Results from kinetic theory model for solid phase constitutive relations are listed in Eqs. (9)–(16), in which the solid phase pressure, Eq. (12) and viscosities, Eqs. (13) and (14) are dependent on the granular temperature, θ. The granular temperature equation is shown in Eq. (5). The gas phase turbulent flow is modeled using a simple sub-grid scale (SGS) model shown in Eqs. (7) and (8).

2.2. Boundary conditions

To solve the equations listed in Table 1, we need appropriate boundary conditions for velocities of the gas and the solids, pressure, and the granular temperature. At the inlet, all velocities and concentrations of both phases are specified. At the outlet, the pressure is at an ambient atmosphere and the mass fluxes of both gas and solids are assumed at continuous. Initially, the gas velocity inside the precalciner is set to zero and there are no particles in the column. At an impenetrable wall, the gas tangential and normal velocities are set to zero (no slip condition). The normal velocity of particles is also set to zero at the wall. The following boundary conditions apply, respectively, for the tangential velocity and granular temperature of the solid phase at the wall [11]:

$$\mathbf{v}_{t,w} = -\frac{6\mu_s\varepsilon_{s,max}}{\pi\rho_s\varepsilon_s g_0\sqrt{3\theta}}\frac{\partial \mathbf{v}_{s,w}}{\partial n} \tag{25}$$

$$\theta_w = -\frac{k_s\theta}{e_w}\frac{\partial\theta_w}{\partial n} + \frac{\sqrt{3}\pi\rho_s\varepsilon_s\mathbf{v}_s g_0\theta^{3/2}}{6\varepsilon_{s,max}e_w} \tag{26}$$

where e_w is the coefficient of restitution at the wall and assumed to be a value of 0.90.

2.3. Computer simulation approaches

The equations listed in Table 1 with boundary conditions were solved numerically using a CFD program. The program used generalizes the previous modified K-FIX code by the addition of body-fitted coordinates. The previous modified K-FIX codes have been used to model the flow in the bubbling fluidized bed and riser [7–9,12]. The original K-FIX program was developed by Rivard and Torrey [19] using the ICE (Implicit Continuum Eulerian) method [20] to solve two-dimensional two-fluid flows. The K-FIX program was developed subsequently for modeling gas–solids fluidizations by Gidaspow research group at Illinois Institute of Technology and demonstrated to be adaptable to variety of problems, e.g. [4,7–9,12].

Table 1
Mathematical model of gas solid flow

A. Conservation laws

(1) Continuity equations

(a) Fluid phase

$$\frac{\partial}{\partial t}(\varepsilon_g\rho_g) + \nabla\cdot(\varepsilon_g\rho_g\mathbf{v}_g) = 0 \quad (1)$$

(b) Particulate phase

$$\frac{\partial}{\partial t}(\varepsilon_s\rho_s) + \nabla\cdot(\varepsilon_s\rho_s\mathbf{v}_s) = 0 \quad (2)$$

(2) Momentum equations

(a) Fluid phase

$$\frac{\partial}{\partial t}(\varepsilon_g\rho_g\mathbf{v}_g) + \nabla\cdot(\varepsilon_g\rho_g\mathbf{v}_g\mathbf{v}_g) = -\varepsilon_g\nabla\mathbf{P}_g + \varepsilon_g\rho_g\mathbf{g} - \beta_{gs}(\mathbf{v}_g - \mathbf{v}_s) + \nabla\cdot\tau_g \quad (3)$$

(b) Particulate phase

$$\frac{\partial}{\partial t}(\varepsilon_s\rho_s\mathbf{v}_s) + \nabla\cdot(\varepsilon_s\rho_s\mathbf{v}_s\mathbf{v}_s) = -\varepsilon_s\nabla\mathbf{P}_g + \nabla\cdot\tau_s + \varepsilon_s\rho_s\mathbf{g} + \beta_{gs}(\mathbf{v}_g - \mathbf{v}_s) \quad (4)$$

(3) Equation of conservation of solids fluctuating energy

$$\frac{3}{2}\left[\frac{\partial}{\partial t}(\varepsilon_s\rho_s\theta) + \nabla\cdot(\varepsilon_s\rho_s\theta)\mathbf{v}_s\right] = (-\nabla\mathbf{P}_s\bar{\mathbf{I}} + \tau_s) : \nabla\mathbf{v}_s + \nabla\cdot(k_s\nabla\theta) - \gamma_s + \phi_s + D_{gs} \quad (5)$$

B. Constitutive equations

(a) Fluid phase stress

$$\tau_g = \mu_g[\nabla\mathbf{v}_g + (\nabla\mathbf{v}_g)^T] - \tfrac{2}{3}\mu_g(\nabla\cdot\mathbf{v}_g)\mathbf{I} \quad (6)$$

(b) Gas shear viscosity (SGS)

$$\mu_g = \mu_{g,l} + \rho_g(0.1\Delta)^2(\Delta\tau_g : \Delta\tau_g) \quad (7)$$

$$\Delta = (\Delta x\Delta y)^{1/2} \quad (8)$$

(c) Solid phase stress

$$\tau_s = (-\mathbf{P}_s + \xi_s\nabla\cdot\mathbf{v}_s)\mathbf{I} + \mu_s\{[\nabla\mathbf{v}_s + (\nabla\mathbf{v}_s)^T] - \tfrac{1}{3}(\nabla\cdot\mathbf{v}_s)\mathbf{I}\} \quad (9)$$

(d) Dissipation fluctuating energy

$$\gamma_s = 3(1-e^2)\varepsilon_s^2\rho_s g_0\theta\left(\frac{4}{d}\sqrt{\frac{\theta}{\pi}} - \nabla\cdot\mathbf{v}_s\right) \quad (10)$$

(e) Radial distribution function at contact

$$g_0 = \left[1 - \left(\frac{\varepsilon_s}{\varepsilon_{s,max}}\right)^{1/3}\right]^{-1} \quad (11)$$

(f) Solid pressure

$$\mathbf{P}_s = \varepsilon_s\rho_s\theta[1 + 2g_0\varepsilon_s(1+e)] \quad (12)$$

(g) Shear viscosity of solids

$$\mu_s = \frac{4}{5}\varepsilon_s^2\rho_s d g_0(1+e)\sqrt{\frac{\theta}{\pi}} + \frac{10\rho_s d\sqrt{\pi\theta}}{96(1+e)\varepsilon_s g_0}\left[1 + \frac{4}{5}g_0\varepsilon_s(1+e)\right]^2 \quad (13)$$

(h) Bulk solids viscosity

$$\xi_s = \frac{4}{3}\varepsilon_s^2\rho_s d g_0(1+e)\sqrt{\frac{\theta}{\pi}} \quad (14)$$

(i) Rate of energy dissipation per unit volume

$$D_{gs} = \frac{d\rho_s}{4\sqrt{\pi\theta}}\left(\frac{18\mu_g}{d^2\rho_s}\right)^2|\mathbf{v}_g - \mathbf{v}_s|^2 \quad (15)$$

(j) Exchange of fluctuating energy between gas and particles

$$\phi_s = -3\beta\theta \quad (16)$$

(k) Fluid–particulate interphase drag coefficients [18]

$$\beta_{gs} = \varphi\beta_{gs}|_{Ergun} + (1-\varphi)\beta_{gs}|_{Wen\,\&\,Yu} \quad (17)$$

$$\varepsilon_g \geq 0.8: \quad \beta_{gs}|_{Wen\,\&\,Yu} = \frac{3}{4}C_D\frac{\rho_g\varepsilon_s|\mathbf{v}_g - \mathbf{v}_s|}{d}\varepsilon_g^{-2.65} \quad (18)$$

$$\varepsilon_g < 0.8: \quad \beta_{gs}|_{Ergun} = 150\frac{(1-\varepsilon_g)\varepsilon_s\mu_g}{(\varepsilon_g d)^2} + 1.75\frac{\rho_g\varepsilon_s|\mathbf{v}_g - \mathbf{v}_s|}{\varepsilon_g d} \quad (19)$$

$$\varphi = \arctan\left(\frac{150\times 1.75(0.2-\varepsilon_s)}{\pi}\right) + 0.5 \quad (20)$$

$$C_D = \frac{24}{Re}(1 + 0.15Re^{0.687}), \quad Re < 1000 \quad (21)$$

$$C_D = 0.44, \quad Re \geq 1000 \quad (22)$$

$$Re = \frac{\rho_g\varepsilon_g|\mathbf{v}_g - \mathbf{v}_s|d}{\mu_g} \quad (23)$$

(l) Ideal gas equation

$$\rho_g = \frac{P}{RT} \quad (24)$$

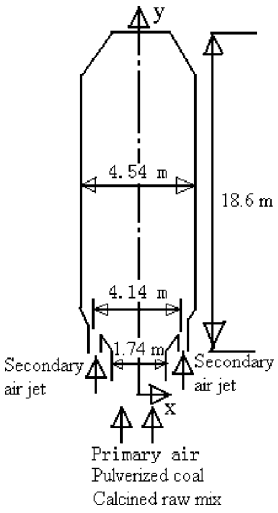

Fig. 1. Illustration of the precalciner geometry.

3. Simulation results and discussions

A typical precalciner used in the cement industry was simulated and analyzed. Fig. 1 illustrates a sketch of the precalciner, which has a capacity about 2000 t per day, with a diameter of 4.54 m and a height of 18.6 m. A mixture of primary air and pulverized coal particles enter the precalciner through the bottom center of the precalciner column, while the secondary air is introduced to the precalciner through the jets located at the conical bottom. The inner diameter of the primary jet is 1.74 m. The secondary jet is located at a distance of 2.07 m from axis, with an inner diameter of 20 mm. The average diameter and density of particles are 30 μm and 1600 kg/m^3, respectively. For a base simulation, the gas velocities from the primary and secondary jets are, respectively, set to 25 and 180 m/s. The solid inlet mass flux from primary jet is 30 kg/m^2 s. The particle–particle coefficient of restitution is set to 0.99, or otherwise specified. For simplicity, a two-dimensional computational domain is assumed in the following simulations with stretched grid of 65×260 nodes and a constant time step of 1.0×10^{-5}. All simulations are continued for 60 s of real simulation time, which require up to 2 weeks of computational time on a PC (20 GB hard disk, 128 Mb RAM, and 600 MHz CPU). All presented time-averaged distributions were taken from 15 to 60 s from simulation results.

Several cases have been modeled in order to investigate the effect of operating conditions on the gas–solid flow pattern in the precalciner. They are presented below.

3.1. Base case simulation results

The base case simulations are performed with the gas velocities from primary and secondary jets are 25 and 180 m/s, respectively. Fig. 2a and b illustrates the computed instantaneous particle concentrations in full- and half-scale columns at the times of 10.0, 15.0, 20.0 and 30.0 s. For the half-scale case computation, the symmetrical flow is assumed along the precalciner axis ($x = 0$), at which the radial velocities of the gas and the solid phases are set to zero. The particles carried by the primary air are injected from bottom into the precalciner by the central jet. The secondary air induced into the precalciner with a much high air velocity forms a dilute jet region. It is observed that there are more particles near the center and less near the walls, and particles

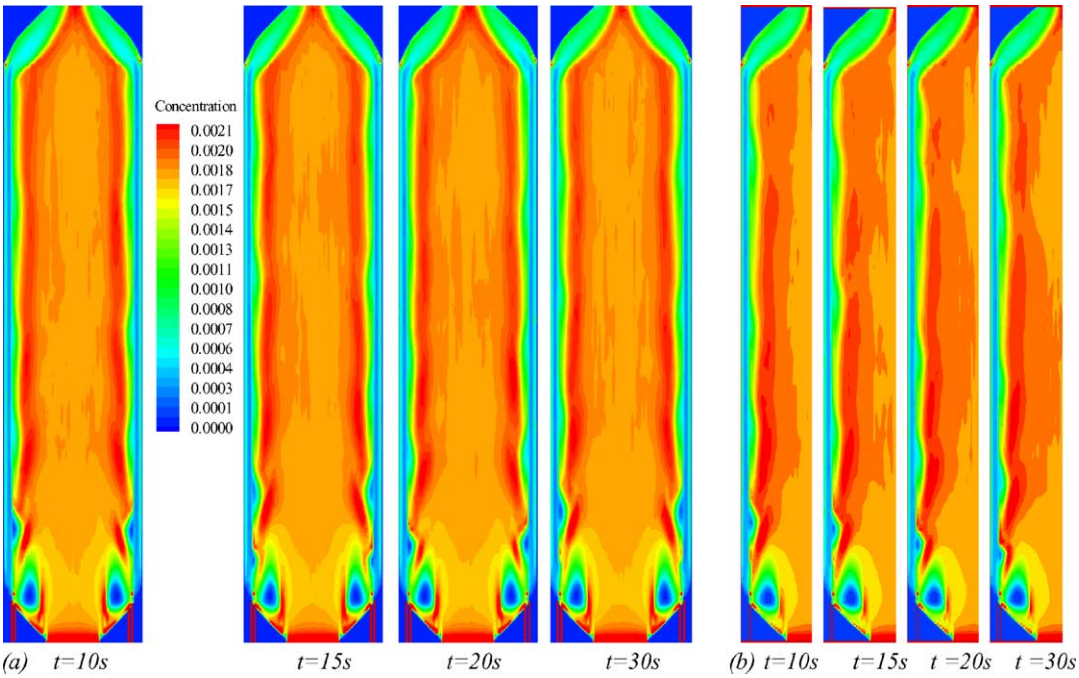

Fig. 2. Instantaneous particle concentration distributions at the velocities of the primary and secondary jets of 25 and 180 m/s.

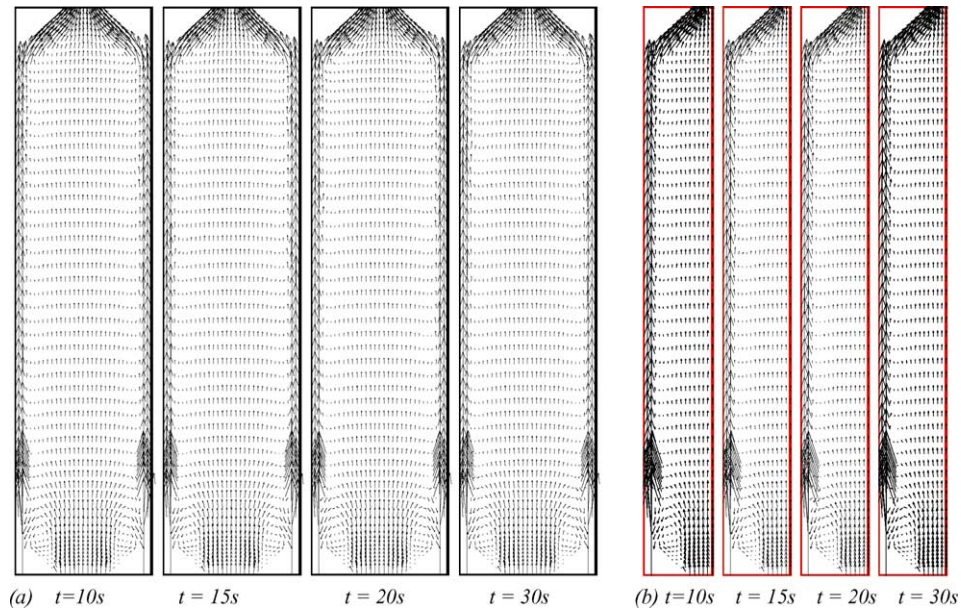

Fig. 3. Instantaneous gas velocity distribution at the velocities of the primary and secondary jets of 25 and 180 m/s.

tend to accumulate in the region between two jets. The particles are non-uniformly distributed in the precalciner. Near the bottom of the precalciner the local region of low particle concentration is formed between two jets. The dilute annulus-dense core flow pattern found in the precalciner is different from the dilute core-dense annulus pattern in the circulating fluidized bed (e.g. [16,17]).

Fig. 3a and b shows the instantaneous gas velocity distribution in full- and half-scale precalciner as a function of time. The gas velocities are high in the center because of primary jet, high near the walls because of the secondary jet, and low between two jets. Near the inlet and in between the two jet entrances, vortexes are observed. Such flow circulations are due to two different inlet jet velocities. These small particle motions are closely follow the gas flows, as shown in Fig. 4a and b. The particles are completely carried up by the induced air jets.

Fig. 5 shows the instantaneous particle concentration at three locations. It is seen that after about 5 s the precalciner filled with particles and both the gas and particle mass fluxes are balanced between outlet and inlet. However, the local particle concentration still oscillates at relatively small magnitudes. Fig. 6 shows the power spectrum density (PSD) distribution of instantaneous particle concentration

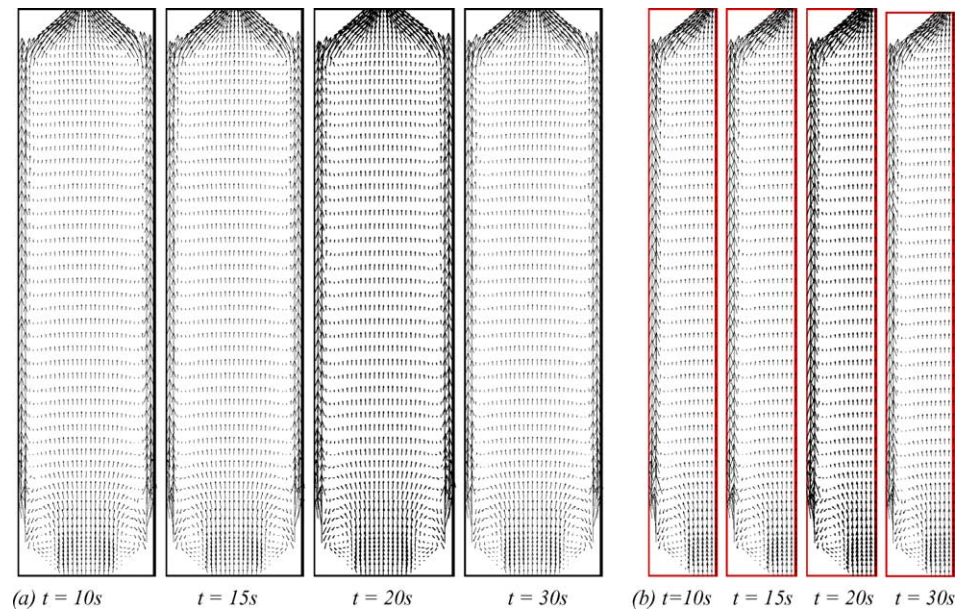

Fig. 4. Instantaneous particle velocity distribution at the velocities of the primary and secondary jets of 25 and 180 m/s.

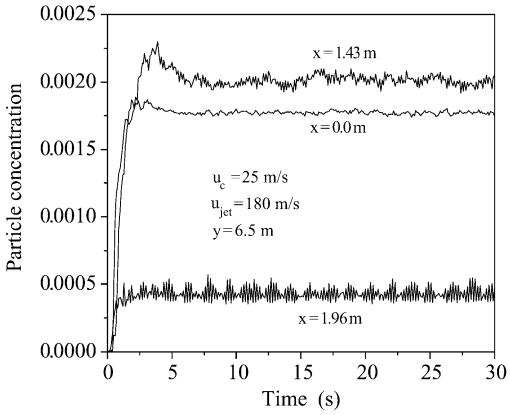

Fig. 5. Instantaneous particle concentration at the velocities of the primary and secondary jets of 25 and 180 m/s.

calculated by Fast Fourier Transformation (FFT) method. It can be seen that the PSD plots of the local particle concentration fluctuation exhibits a broad-band characteristics with many spikes over a wide frequency range. It is noticed that more significant particle temporal fluctuations neat the wall ($x = 1.96$ m) and the region between two jets ($x = 1.43$ m) than that at the center ($x = 0$). It can be conclude that the primary and secondary jets play important role on the gas–solid flow behavior in the precalciner.

Fig. 7 shows the time-averaged particle concentration distributions at four locations. The particle concentration is high near the center. The particle concentration decreases, reaches a minimum, and then increases at the walls. It is clear that particles diffused away from center of the primary jet region to the walls. Such phenomena are caused combined with two jet diffusion effects. Near the center, the particle distribution is quite uniform. The maximum particle concentration is located somewhere between $x/D = 0.3$ and 0.34. The aerations of the jets lead to a low particle concentration between the two jets. At a height of 1.66 m, the particle concentration is down to a minimum at $x/D = 0.3$.

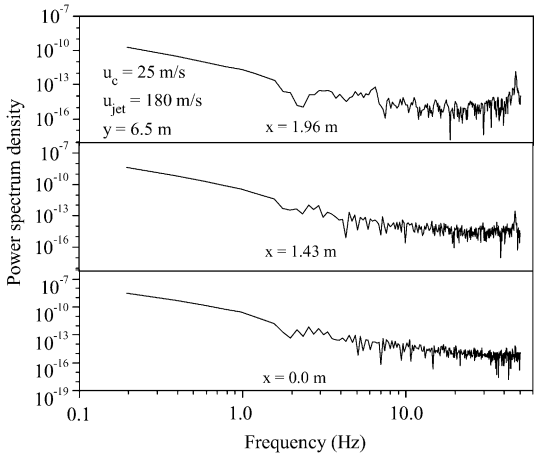

Fig. 6. Power spectrum density of instantaneous particle concentration at the velocities of the primary and secondary jets of 25 and 180 m/s.

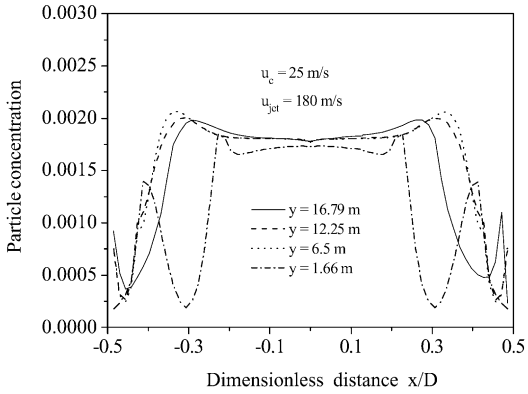

Fig. 7. Time-averaged concentration at the velocities of the primary and secondary jets of 25 and 180 m/s.

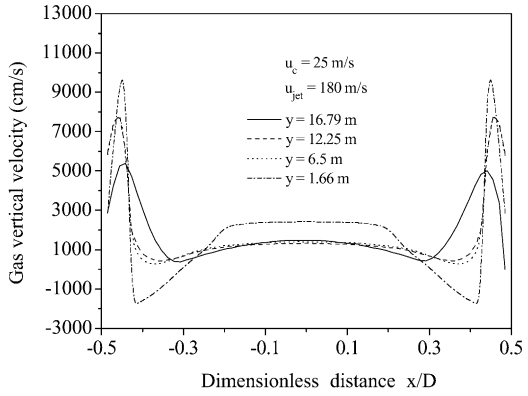

Fig. 8. Time-averaged gas velocity at the velocities of the primary and secondary jets of 25 and 180 m/s.

The computed time-averaged gas and particle velocity distributions are shown in Figs. 8 and 9, respectively. Due to high secondary jet velocity, both the gas and solids velocities are high near the walls. At the center gas velocity is low. The gas velocities at a height of 12.25 m are almost the same as those at a height of 6.5 m. The solids velocity is similar to the gas velocity distribution at these heights. The gas–solids flow above the height of 6.5 m becomes developed. The negative velocities near the jet entrances are due

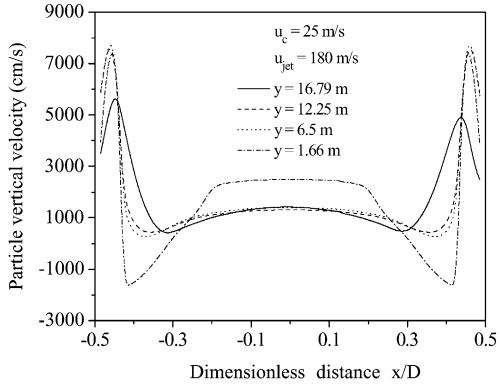

Fig. 9. Time-averaged particle velocity at the velocities of the primary and secondary jets of 25 and 180 m/s.

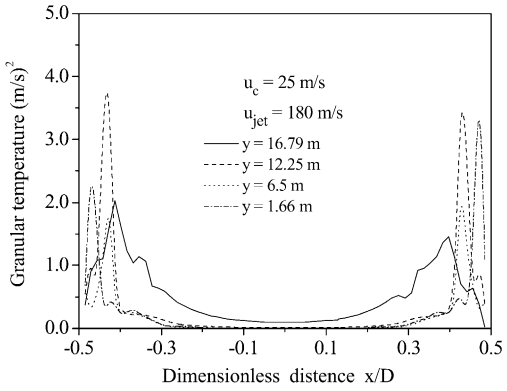

Fig. 10. Time-averaged granular temperature at the velocities of the primary and secondary jets of 25 and 180 m/s.

to the flow circulations or vortexes between the two jets, as indicated in Fig. 3a and b.

The computed granular temperature distribution is shown in Fig. 10. The simulated results show a high fluctuating velocity near the walls and at the region between two jets. Since the higher solids shear rates are expected near the regions, where solid phase velocities are so different between the two jets and between the walls and locations near the walls, it is not surprised that more significant particle–particle collisions occur at these regions caused by the shear rates, hence the granular temperature is higher than other regions.

3.2. Effect of secondary jet velocity

Fig. 11 shows the time-averaged particle concentration as a function of the secondary jet velocity at a constant primary jet velocity of 25 m/s. For the case of the secondary jet velocity at 100 and 130 m/s, the particle concentration decreases in the radial direction, and down to a minimum at the walls. For the case of the secondary jet velocities at 180 and 210 m/s, the particle concentrations are at a maximum near $x/D = \pm 0.34$ between two jets, at minimum near $x/D = \pm 0.44$, then gradually increases at the walls. Fig. 12 shows particle velocity distribution as a function of the secondary jet velocity. The vertical solids velocity decreases

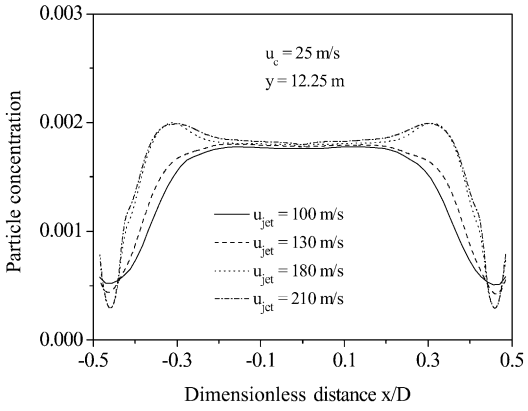

Fig. 11. Time-averaged concentration at the primary jet velocity of 25 m/s.

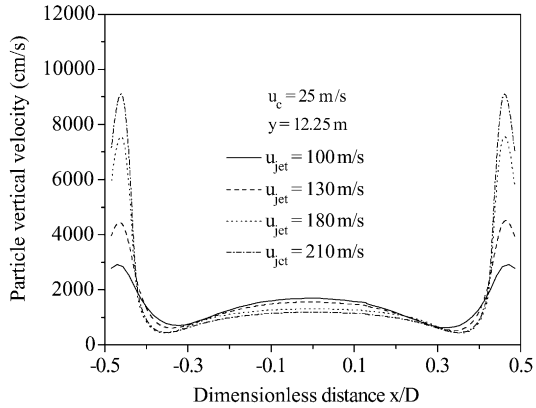

Fig. 12. Time-averaged particle velocity at the primary jet velocity of 25 m/s.

gradually toward the walls, reaches a minimum at the region between two jets, then increases at the walls. The maximum vertical velocity of particles decreases with the decrease of secondary jet velocity. Comparing Fig. 12 with Fig. 11, it is noticed that the lower particle velocity is corresponding to the higher particle concentration.

3.3. Effect of primary jet velocity

The influence of primary jet velocity on particle concentration and velocity are shown, respectively, in Figs. 13 and 14 with a fixed secondary jet velocity of 180 m/s while the solids mass flux keeps at 30 kg/m^2 s. It is noted that the maximum particle concentrations are away from center and somewhere between the two jets. Such a phenomenon may be due to the results of two jet interactions. However, increasing the primary jet velocity will flat the particle distributions, as shown in Fig. 13. The particle concentration increases with decrease of primary jet velocity in the center of the precalciner column. From Figs. 13 and 14, it is found that the maximum particle velocities and minimum particle concentrations are in the secondary jet region.

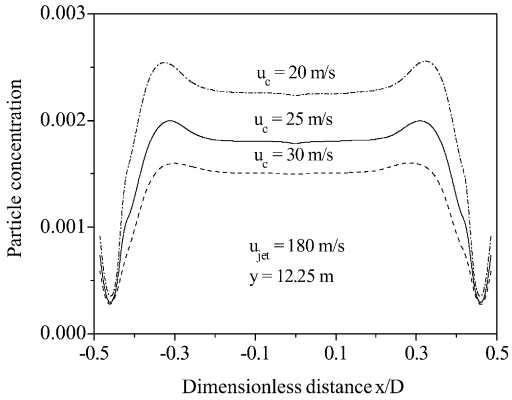

Fig. 13. Time-averaged concentration at the secondary jet velocity of 180 m/s.

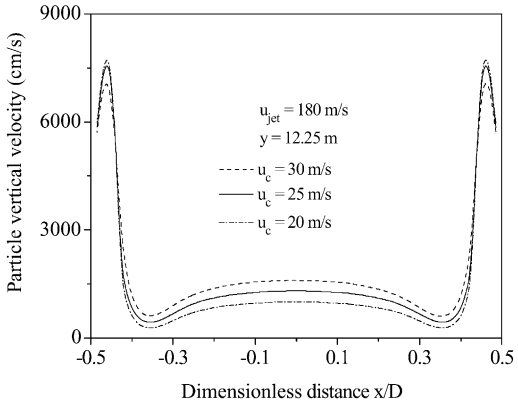

Fig. 14. Time-averaged particle velocity at the secondary jet velocity of 180 m/s.

3.4. Effect of secondary jet arrangement

Fig. 15 shows the time-averaged particle concentration distributions as a function of the secondary jet location at the velocities of primary and secondary jets of 25 and 180 m/s, respectively. As the location of secondary jet more close to the center, the maximum particle concentration becomes closer to the center, even though the peak of the maximum particle concentration is less obvious for the case of the secondary jet at 1.70 m away from the center. As expected, the locations of minimum particle concentration shift following the secondary jet location change. The value of the particle concentration at the wall increases as the secondary jet moves away from the wall. The corresponding time-averaged particle velocity as a function of the secondary jet location is shown in Fig. 16. The particle velocity decreased at the wall as the secondary jet moves away from the wall. At the same location, the higher particles concentration is, the lower particle velocity, or vice versa.

3.5. Effect of inlet particle mass flux from primary jet

Figs. 17 and 18 show, respectively, the time-averaged radial and vertical particle concentrations as a function of

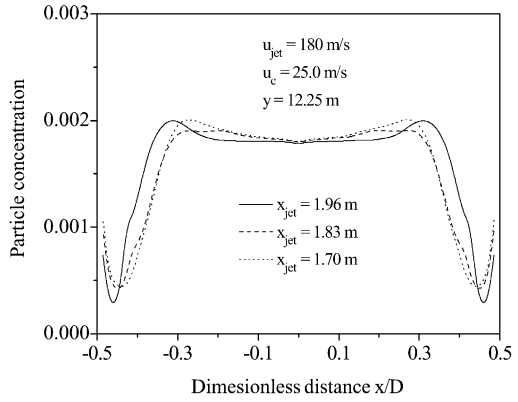

Fig. 15. Time-averaged particle concentration at the secondary jet velocity of 180 m/s.

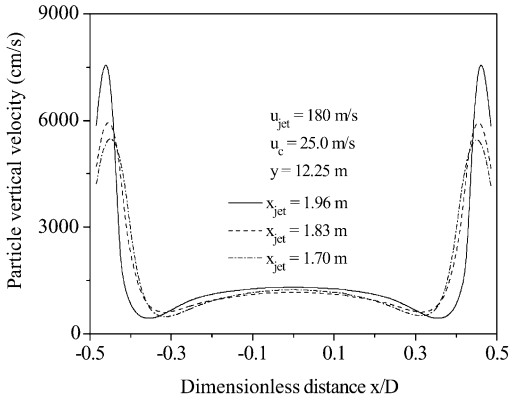

Fig. 16. Time-averaged particle velocity at the secondary jet velocity of 180 m/s.

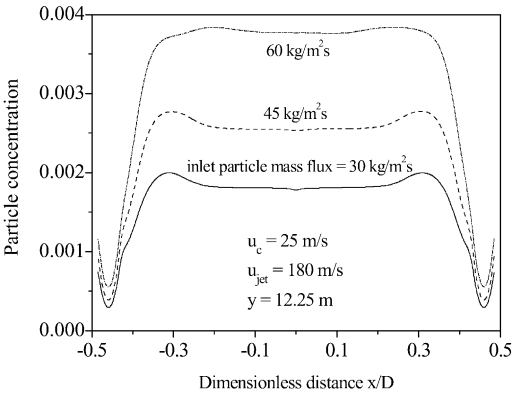

Fig. 17. Time-averaged radial particle concentration profile.

inlet particle mass flux under conditions of constant primary jet velocity of 25 m/s and the secondary jet velocity of 180 m/s. It is not surprise that the particle concentrations increase with the increase of particle mass flux. The vertical particle concentrations, shown in Fig. 18, are presented in cross-section averaged distribution alone the precalciner height. For all cases of particle mass fluxes presented, the particle concentrations change gradually from bottom to a height of 5.0 m. After that height, the particle concentrations become almost constant before outlet, where particle

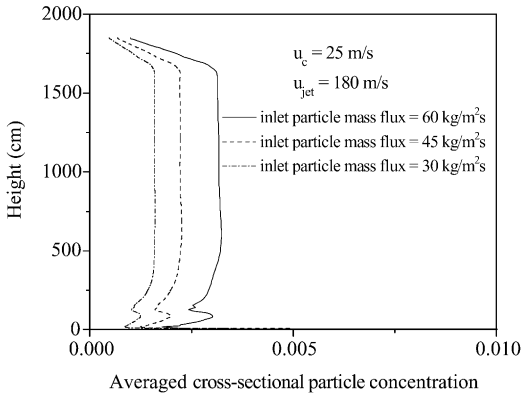

Fig. 18. Time-averaged cross-sectional concentration profile.

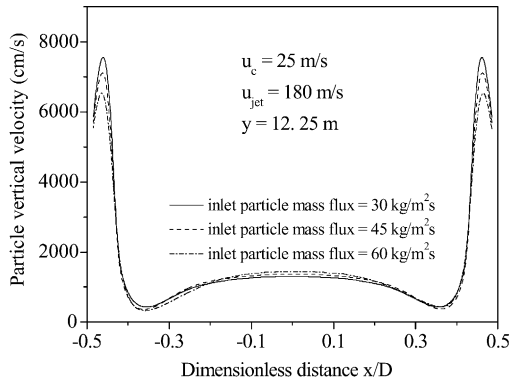

Fig. 19. Time-averaged particle velocity at the secondary jet velocity of 180 m/s.

concentrations become lower in response to the flow area contraction. These types of particle distributions are related to the flow development in the precalciner as well as inlet and outlet geometry change. Fig. 19 shows the particle vertical velocity at height of 12.25 m as a function of the inlet particle mass flux. Since the particle velocity is dominated by the carrying gas flow, there is no much difference of the solids velocities for various inlet solids mass fluxes. However, the radial solids mass flux profiles do display significant differences because of particle concentration distribution variations in the precalciner, as shown in Fig. 20.

3.6. Effect of coefficient of restitution

As the coefficient of restitution increases, particle–particle collisions become more elastic and less fluctuating energy dissipation during collisions. Hence, the simulated granular temperature tends to increase as the coefficient of restitution increases. This, in turn, results in higher solids viscosity and pressure hence modulations the hydrodynamics of gas–solids flow. Fig. 21 shows the time-averaged granular temperature distribution changes with the coefficient of restitution. The alternation of particle distribution by coefficient of restitution is demonstrated in Fig. 22.

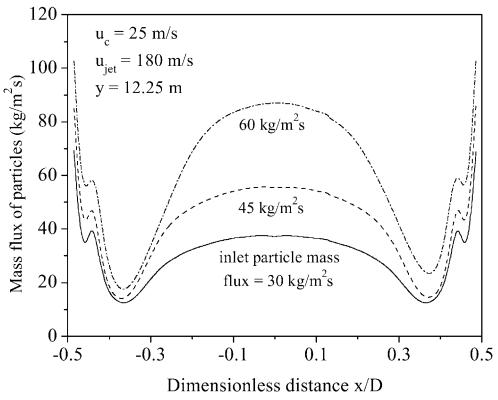

Fig. 20. Time-averaged mass flux of particle at the secondary jet velocity of 180 m/s.

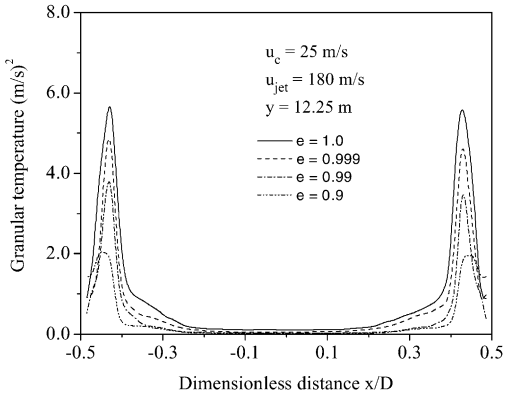

Fig. 21. Granular temperature distribution as a function of coefficient of restitution at the velocities of the primary and secondary jets of 25 and 180 m/s.

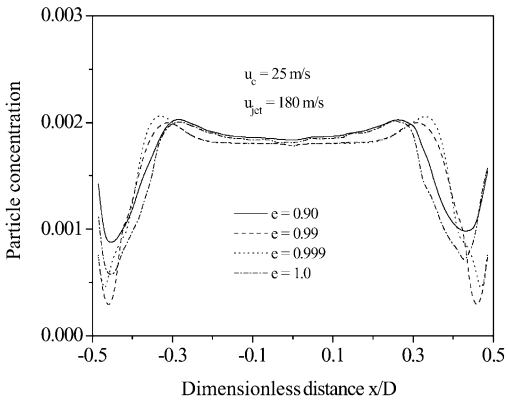

Fig. 22. Particle concentration as a function of coefficient of restitution at the velocities of the primary and secondary jets of 25 and 180 m/s.

4. Conclusion

The hydrodynamic behavior of a gas–solid flow in the precalciner was simulated using a two-fluid model incorporated with the kinetic theory of granular flow. The numerical simulations illustrate the ability of present computer model to represent gas–solid flow in the precalciner. The dilute annulus-dense core structure is well predicted which is dissimilar to dilute core-dense annulus flow structure in the riser of circulating fluidized bed.

The influence of the precalciner operation conditions, such as the jet velocities of the primary and secondary inlet and inlet mass flux, on gas–solids flow hydrodynamics was demonstrated from computer simulations. It is possible to use the present computer simulation approaches to obtain the optimal performance of the precalciner by selecting the operation parameters. The effects of the secondary jet arrangement are significant in the overall gas–solid flow patterns in the precalciner as well. The present two-dimensional simulation computer code may be used as tool for guiding the jet arrangement design, although actual inlet jet

geometry arrangement has to be modeled designed by three-dimensional simulations.

The present simulations showed the effects of the coefficient of restitution of particle–particle collisions on gas–solids flow. Appropriate coefficients of restitution for particle–particle and particle-wall collisions, which may have to be determined from tedious experiments and investigations, are needed to obtain more accurate simulation results.

Acknowledgements

This work was supported by the Key Laboratory for Silicate Materials Science and Engineering of Ministry of Education of Wuhan University of Technology under grant no. MD2002.31.

References

[1] I. Iliuta, K. Dam-Johansen, L.S. Jensen, Mathematical modeling of an in-line low-NO_x calciner, Chem. Eng. Sci. 57 (2002) 805–820.
[2] D.S. Lee, J.M. Pacyna, An industrial emissions inventory of calcium for Europe, Atmos. Environ. 33 (1999) 1687–1697.
[3] S.L. Soo, Fluid Dynamics of Multiphase Systems, Blaisdell-Ginn, Waltham, MA, 1967.
[4] D. Gidaspow, Multiphase Flow and Fluidization: Continuum and Kinetic Theory Description, Academic Press, San Diego, 1994.
[5] C. Crowe, M. Sommerfeld, T. Tsuji, Multiphase Flows with Droplets and Particles, CRC Press, Boston, 1998.
[6] R. Jackson, Progress toward a mechanics of dense suspensions of solid particles, AIChE Symp. Ser. 90 (1993) 1–14.
[7] Y.P. Tsuo, D. Gidaspow, Computation of flow patterns in circulating fluidized beds, AIChE J. 36 (1990) 885–896.
[8] B. Sun, D. Gidaspow, Computation of circulating fluidized bed riser flow for the fluidization. VIII. Benchmark test, Ind. Eng. Chem. Res. 38 (1999) 787–792.
[9] L. Huilin, D. Gidaspow, Hydrodynamic simulations of gas–solid flow in a riser, Ind. Eng. Chem. Res. 42 (2003) 2390–2398.
[10] S. Chapman, T.G. Cowling, The Mathematical Theory of Non-uniform Gases, 3rd ed., Cambridge University Press, Cambridge, 1970.
[11] J.L. Sinclair, R. Jackson, Gas–particle flow in a vertical pipe with particle–particle interactions, AIChE J. 35 (1989) 1473–1486.
[12] J. Ding, D. Gidaspow, A bubbling fluidization model using kinetic theory of granular flow, AIChE. J. 36 (1990) 523–538.
[13] J. Pita, S. Sundaresan, Developing flow of a gas–particle mixture in a vertical riser, AIChE J. 39 (1993) 541–552.
[14] E.J. Bolio, J.L. Sinclair, Gas turbulence modulation in the pneumatic conveying of massive particles in vertical tubes, Int. J. Multiphase Flow 21 (1995) 985–1001.
[15] J.J. Nieuwland, M. van sint Annaland, J.A.M. Kuipers, W.P.M. van Swaaij, Hydrodynamic modelling of gas/particle flows in riser reactors, AIChE J. 42 (1996) 1569–1582.
[16] S. Benyahia, H. Arastoopour, T.M. Knowlton, H. Massah, Simulation of particles and gas flow behavior in the riser section of a circulating fluidized bed using the kinetic theory approach for the particulate phase, Powder Technol. 112 (2000) 24–33.
[17] A. Neri, D. Gidaspow, Riser hydrodynamics: simulation using kinetic theory, AIChE J. 46 (2000) 52–67.
[18] L. Huilin, D. Gidaspow, J. Bouillard, L. Wentie, Hydrodynamic simulation of gas–solid flow in a riser using kinetic theory of granular flow, Chem. Eng. J. 95 (2003) 1–13.
[19] W.C. Rivard, M.D. Torrey, K-FIX: a computer program for transient, two dimensional, two fluid flow, LA-NUREG-6623, Los Alamos National Laboratory, Los Alamos, 1977.
[20] F.H. Harlow, A.A. Amsdende, Numerical calculation of multiphase flow, J. Comput. Phys. 17 (1975) 19–52.